



Photocatalytic degradation and mineralization of dye pollutants from wastewater under visible light using synthetic CuO-VO₂/TiO₂ nanotubes/nanosheets

Z. Moradi Shammi¹, AH. Kianfar^{1,2,*} , and M. M. Momeni²

¹Department of Chemistry, Isfahan University of Technology, 84156/83111 Isfahan, Iran

²Isfahan University of Technology, 84156/83111 Isfahan, Iran

Received: 16 February 2021

Accepted: 22 June 2021

Published online:

21 July 2021

© The Author(s), under exclusive licence to Springer Science+Business Media, LLC, part of Springer Nature 2021

ABSTRACT

CuO-VO₂/TiO₂ as a new nanocomposite was synthesized through hydrothermal method and identified by various spectroscopic techniques including X-ray diffraction (XRD), X-ray photoelectron spectroscopy (XPS), scanning electron microscopy (SEM), high-resolution transmission electron microscopy (HR-TEM), energy dispersive X-ray analysis (EDX), UV–visible, differential reflectance spectroscopy (DRS), and Mott–Schottky. The presence of nanotubes/nanosheets in the synthesized nanocomposite was confirmed by HR-TEM. The anatase and rutile crystalline forms of TiO₂ were detected by Raman spectroscopy and X-ray diffraction (XRD). XPS analysis confirmed the presence of CuO and VO₂ in the nanocomposite. The surface area and the band-gap energy of the nanocomposite were determined via N₂ adsorption–desorption analysis and DRS. The presence of a p–n junction between TiO₂ (n-type) and CuO/VO₂ (p-type) was confirmed by the Mott–Schottky analysis. The photocatalytic activity of the nanocomposite against methylene blue (MB), methyl orange (MO), and cango red (CR) was studied under visible-light irradiation. The times of degradation for the decomposition of the dyes were 10–25 min. The rate constants of degradation for MB, MO, and CR were calculated as 0.34, 0.090, and 0.155 min⁻¹, respectively. The catalyst was recovered four times. In addition, the mineralization of the dyes was investigated by chemical oxygen demand (COD). The reaction was performed in the presence of different radical scavengers, and the ·OH was found to be the predominantly active species in the photodegradation of the dyes.

Address correspondence to E-mail: akianfar@cc.iut.ac.ir

1 Introduction

The residual wastewaters from textile, chemical, and leather industries are mostly composed of remarkable quantities of organic dye contaminants, which lead to irrecoverable damage to the environment and human health [1, 2]. The conventional methods for the removal of these pollutants include sedimentation [3], ion flotation [4], coagulation [5], and adsorption [6]. However, these methods suffer from the production of secondary wastes, which require further processing. Advanced oxidation processes (AOPs) are one of the rather new and stronger techniques developed for the removal of dye contaminants from wastewater [7]. AOPs basically generate reactive hydroxyl radical ($\cdot\text{OH}$) as powerful oxidizing agents for a broad range of pollutants and oxidize them in a quick and non-selective manner [8]. The hydroxyl radical is generally produced by chemical and photochemical processes [9, 10]. Photochemical oxidation of organic dyes is an effective treatment method applied to remove organic dyes from wastewater. It is clear that the source of light is important because of energy saving and environmental pollution considerations. In most of photochemical reports, the source of energy is UV irradiation generated in situ [11]. Titanium dioxide (TiO_2) photocatalyst has been generally applied in photocatalytic oxidation of many organic dyes such as MB, MO, and CR [12]. This compound has a low production cost, outstanding photocatalytic activity, non-toxicity, and high photocorrosion resistance [13]. Therefore, this compound is commercially available as an active photocatalyst for the decomposition of dyes. However, given its high band gap (3.2 eV), it is only active under UV irradiation and applicable in closed containers [14]. Most of the dye production wastewater is released into the environment. Many efforts have been made to modify TiO_2 and make it active in visible light [15]. Metal oxides doped on TiO_2 and nanocomposites are expected to show various effects on the photocatalytic activity of TiO_2 by different methods. Many metal ions including iron [16], palladium [17], nickel [18], copper [19], silver [20], vanadium [21], cobalt [22], and platinum [23] have been studied as potential dopants. Metal ions doped into TiO_2 can presumably enhance the electronic energy band structure of TiO_2 and, thus, improve its photocatalytic performance by the

efficient charge transfer from the doped metal ions to Ti^{4+} . It is worthwhile to study the method of doping TiO_2 , an n-type semiconductor with wide band gap, with semiconductors such as p-type semiconductors (with narrow band gap) in more detail [24]. For instance, NiO loading could improve the UV–Vis light absorption and then increase the photoelectrochemical and photocatalytic efficacy of TiO_2 due to the generation of a p–n junction during metal oxide loading, which prevents the recombination of photogenerated electron–hole pairs [25]. Copper oxide (CuO) and vanadium (IV) dioxide (VO_2) are important p-type semiconductors, which have specific band gaps of nearly 2.0 and 2.6 eV, respectively. CuO and VO_2 have been considered p-type semiconductors joined with n-type TiO_2 semiconductors in many photocatalytic studies due to their potential applications in the degradation of organic contaminants. However, there are no reports on doping TiO_2 with CuO– VO_2 mixed metal oxides [26–28]. TiO_2 -based nanocomposites have been prepared by various synthetic methods including hydrothermal, solvothermal, sol–gel, direct oxidation, chemical vapor deposition (CVD), electrodeposition, sonochemical, and microwave [28–30]. Some of the advantages of hydrothermal method compared with other conventional methods are low reaction temperature, prevention of additional thermal treatments, generation of well-crystallized, porous compounds, and low loss. In a typical hydrothermal process, TiO_2 nanoparticles or titanium alkoxides are completely mixed with 10–15 mol/L NaOH. The mixtures, thus, obtained are then heated at 110–180 °C for 16–72 h in a Teflon-lined autoclave. Upon completion of the hydrothermal treatment, the precipitate obtained is washed with deionized water, dispersed in HCl solution, and calcined at 364 °C to obtain well-defined nano- TiO_2 [30]. The morphology of TiO_2 obtained is dependent on such process parameters as the structure of the starting material, alkaline solution concentration, reaction temperature, time, and the effect of washing acid, which suggests the controllability of the synthetic process. The preparation of nanocomposite by hydrothermal method forms various morphologies such as nanostructures, nanotubes, nanowires, nanorods, and mesoporous, which make the studies on nanostructural synthesis and their applications very interesting. Nanotubes and nanosheets are of utmost attraction in photocatalytic applications among these

morphologies given their high surface-to-volume ratios, high surface area, good charge transport properties, and chemical stability [30, 31]. In our lab, many works have been done to modify titanium dioxide by different compounds through the reduction of its band gap to absorb visible light. In these works, the photocatalytic properties of metal oxides and mixed oxides of metal like CuO, NiO, V₂O₅, and CuO-CoO, and the impact of metal complexes morphology of TiO₂ and enhancement of its photocatalytic and catalytic activities have been studied [32–35]. In continuation of our research on mixed metal oxides, two metal oxides (CuO and VO₂) have been doped on TiO₂. In addition, complexes, which do not contain nitrogen such as Cu(acac)₂ and VO(acac)₂, were selected as primary salts. Therefore, CuO-VO₂/TiO₂ nanocomposite (a p-n type semiconductor) has been synthesized by reaction of Cu(acac)₂ and VO(acac)₂ complexes with TiO₂ via hydrothermal method, and the obtained products have been characterized by different spectroscopy techniques including SEM, XRD, Raman XPS, HR-TEM, DR-UV-Vis, Mott-Schottky, and N₂ adsorption-desorption analyses. Methylene blue, methyl orange, and cango red were applied as pollutants to investigate the photocatalytic activity of the novel composite under the visible-light irradiation. In addition, the efficiency of dye mineralization has been estimated by COD.

2 Experimental

2.1 Materials and characterizations

Chemicals containing sodium hydroxide, VO(acac), Cu(acac)₂, Methylene blue (MB), Methyl orange (MO), and cango red (CR) were purchased from Sigma Aldrich Chemical Co. TiO₂ (P-25) nanoparticles were obtained from Hanau-Wolfgang Co. (Germany).

All instruments used in this study for sample characterization were the same as those in our previous publication and presented in S1 section [35].

2.2 Preparation of CuO-VO₂/TiO₂ nanocomposite

CuO-VO₂/TiO₂ nanocomposite was prepared through hydrothermal method using TiO₂ (P-25)

(Degussa) and vanadium(IV) and copper(II) acetylacetonates. First, 0.5 g of TiO₂ nanoparticles (P-25) and 0.5 mmol of Cu(acac)₂ and VO(acac)₂ were dispersed in a solution of NaOH (50 mL 10 M) by magnetic stirrer at 50 °C for 60 min. Afterwards, the suspension obtained was transferred into a autoclave in which it was heated at 180 °C for 24 h. The reaction mixture was then cooled, and the product was treated by 50 mL of 0.1 M HCl overnight. The precipitates were washed via distilled water, dried at 80 °C, and finally calcined in air at 400 °C for 5 h at a heating rate of 2 °C/min. The obtained product was then labeled as CuO-VO₂/TiO₂ nanocomposite [35, 36], Scheme 1.

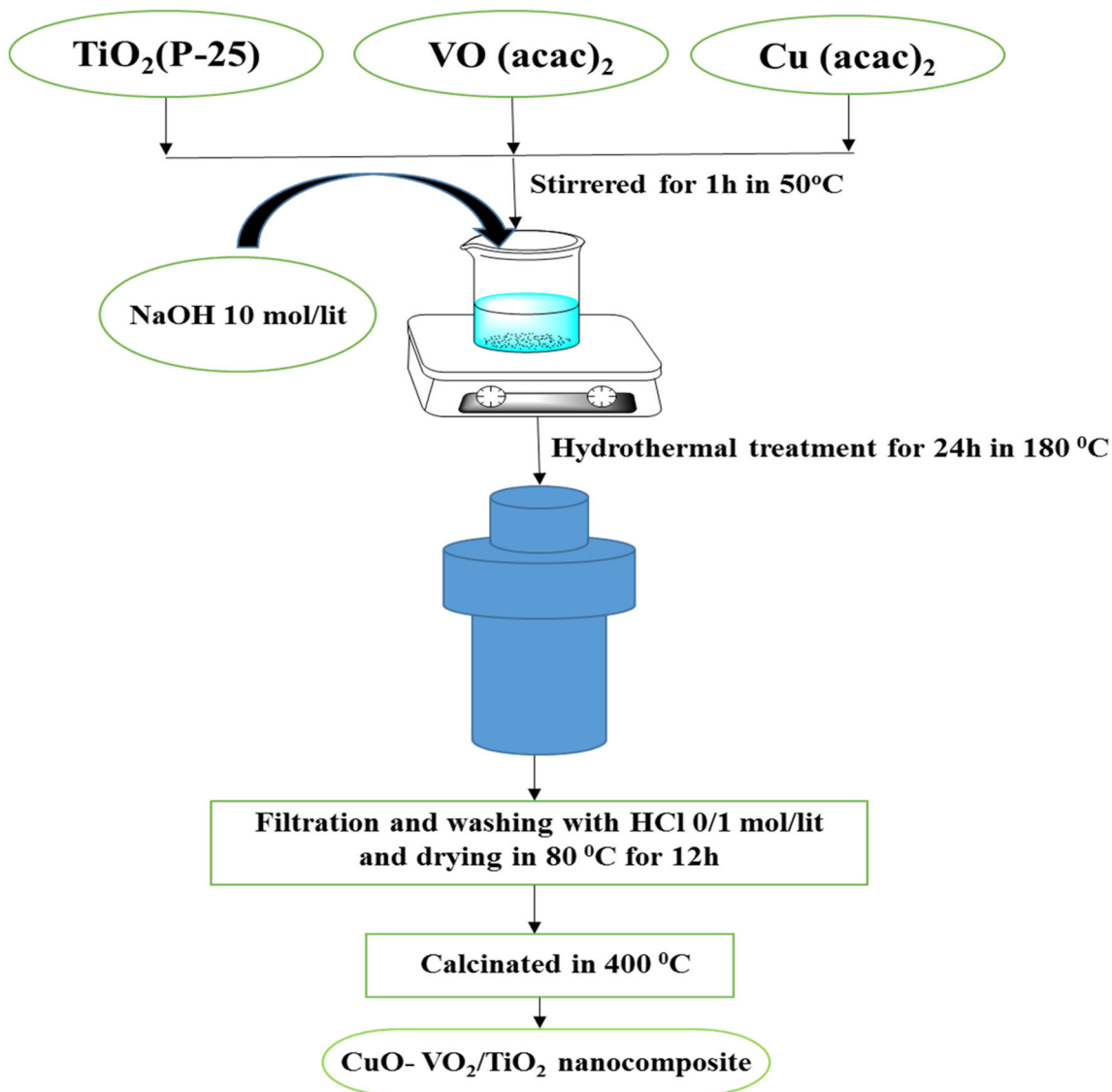
2.3 Photocatalytic activity of CuO-VO₂/TiO₂ nanocomposite under visible-light irradiation

2.3.1 Photodegradation of MB, MO and CR

Stock solutions of the dyes (100 ppm) in double-distilled water were used to prepare 10 ppm working solutions. For heterogeneous photodegradation, 3 mg of CuO-VO₂/TiO₂ nanocomposite was added to dye (5 mL, 10 ppm) in the presence of 1 mL of 0.1 M H₂O₂. The sample was stirred under tungsten lamp (500 W) as source of visible light. The light intensity was 200 mW/cm². A Digital Luxmeter (LX-1010B) was used to measure the intensity and calibrate the light source. The lamp was located at 20 cm from the reaction container. All of photocatalytic tests were done at room temperature and the natural dye pH. The reaction progress was followed by UV-Vis spectroscopy. The maximum absorbance values measured for MB, MO, and CR were 50, 450, and 500 nm, respectively. The disappearance of chemical oxygen demand (COD) indicated the complete mineralization of the dyes. Standard methods were used to estimate COD. The following expressions were used to assess the efficiency of dye mineralization [37]:

$$\text{Mineralization \%} = \left[1 - \frac{\text{COD}}{\text{COD}_0} \right] \times 100, \quad (1)$$

where COD and COD₀ correspond to COD values at time *t* and initial conditions, respectively.



Scheme 1 Schematic representation of the synthesis of CuO-VO₂/TiO₂ by hydrothermal method

2.3.2 Radical scavenger tests

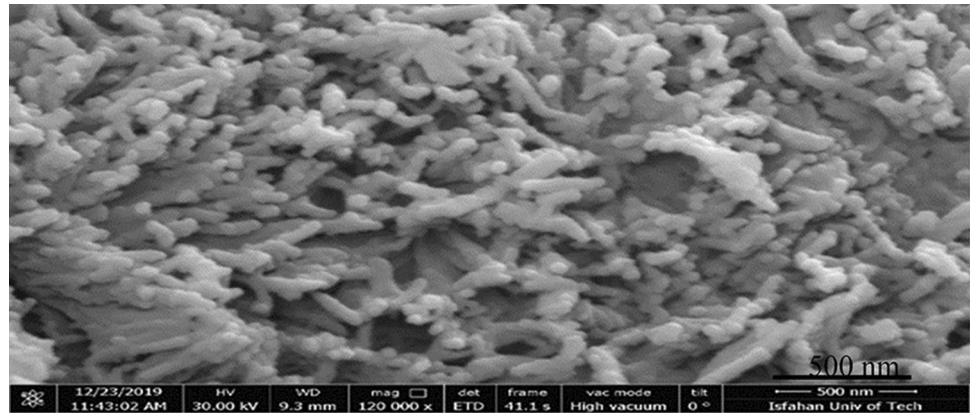
As same as the reported procedure in our last work, the ethylenediaminetetraacetic acid (EDTA), p-benzoquinone (BQ), and isopropyl alcohol (IPA) were selected as radical scavengers for hydroxyl radicals ($\cdot\text{OH}$), superoxide radicals ($\cdot\text{O}_2^-$), and holes (h^+), respectively. In this work, the effect of these scavengers on CuO-VO₂/TiO₂ nanocomposite was assessed. For each dye, 1 mmol of the scavenger, 3 mg of the catalyst, 5 mL of an aqueous solution of the dye (10 ppm), and 1 mL of H₂O₂ (0.1 M) were used to prepare a solution under irradiation by visible light at ambient temperature [38, 39].

3 Results and discussion

3.1 FE-SEM, EDX, and mapping

The morphology of new nanocomposite characterized via FE-SEM. Figure 1 shows the FE-SEM image of the surface of CuO-VO₂/TiO₂ nanocomposite. The morphology of the particles was characterized as nanotube/nanosheet like. The EDX spectra of the TiO₂(P-25) and CuO-VO₂/TiO₂ nanocomposite are shown in Fig. S1 (a and b). The spectrum indicates the presence of V, Ti, O, and Cu. The elemental distribution maps of Cu (red), V (green), Ti (White), and O (gray) are shown in Figs. S2 (a–d), respectively. The presence of Cu and V on the TiO₂ nanotube and

Fig. 1 FE-SEM image of a CuO-VO₂/TiO₂ nanocomposite



nanosheet surface was verified by the element distribution map analysis [40, 41].

3.2 X-ray diffraction

Figure 2 shows the XRD patterns for TiO₂ (P-25) nanoparticles and CuO-VO₂/TiO₂ nanocomposite. In bare TiO₂ (P-25) spectrum, all diffraction peaks are attributed to the crystal planes of phase purity of anatase. The XRD pattern of CuO-VO₂/TiO₂ nanocomposite was observed as rutile at $2\theta = 27.00(101)$, $35.00(011)$, $43.82(120)$, $62.33(022)$, and $63.70(130)$ and anatase at $2\theta = 25.15(101)$, $38.31(103)$, $47.78(020)$, and $54.75(105)$ phase (JCPDS files No. 00-01-0562 and 01-088-1173 for anatase and rutile, respectively). The pure anatase phase of (TiO₂ (P-25)) converted to mixed phase of anatase and rutile in CuO-VO₂/TiO₂ nanocomposite. Diffraction peaks at $2\theta = 34.24(001)$, $37.220(111)$, $40.120(200)$ and

$2\theta = 29.75(110)$, $59.88(220)$, $68.75(301)$ are attributed to CuO and VO₂, respectively (JCPDS files No. 01-078-0428 and 01-076-0675 for CuO and VO₂, respectively) [42, 43].

3.3 Raman spectroscopy

Figure 3 shows the Raman spectra for TiO₂ (P-25) nanoparticles and CuO-VO₂/TiO₂ nanocomposite. For TiO₂ (P-25) nanoparticles, the peaks at 153 (E_g), 407(B_{1g}), 520 (E_g), and 650 (A_{1g}) cm⁻¹ were corresponded to the anatase phase and the peaks at 244 (second-order Raman scattering), 454 (E_g), and 612 (A_{1g}) cm⁻¹ are the typical peaks of the rutile phase. These results indicate that CuO-VO₂/TiO₂ nanocomposite possesses anatase and rutile phases and confirm the XRD results [44]. In addition, compared with the undoped TiO₂ (P-25), given the phonon confinement effect and the strain due to the

Fig. 2 The XRD patterns of (a) TiO₂ (P-25) nanoparticles (b) CuO-VO₂/TiO₂ nanocomposite

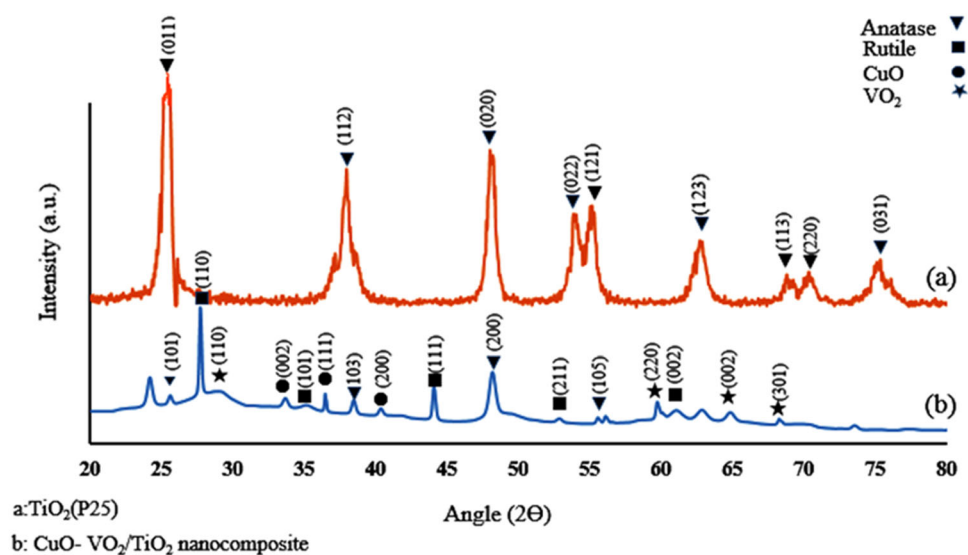
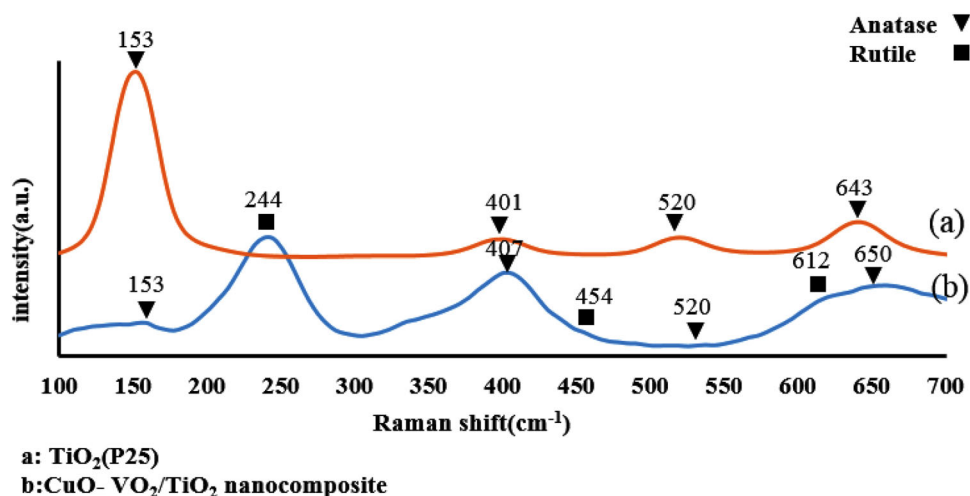


Fig. 3 The Raman spectra of (a) TiO₂ (P-25) and (b) CuO-VO₂/TiO₂ nanocomposite



surface coating, two blue shifts are observed by the peaks at 401 and 643 cm⁻¹ for CuO-VO₂/TiO₂ nanocomposite [45]. On the other hand, the peak intensity and sharpness of all the peaks have reduced in comparison with the undoped TiO₂ (P-25) [46].

3.4 X-ray photoelectron spectroscopy

Figure 4a illustrates the further XPS measurements of CuO-VO₂/TiO₂ nanocomposite. The spectrum of CuO-VO₂/TiO₂ nanocomposite shows the peaks corresponding to Ti, O, Cu, and V. Based on Fig. 4b, the peaks at 458.50 and 464.50 eV are related to Ti2p_{3/2} and Ti2p_{1/2}, respectively, confirming the presence of Ti⁴⁺. The peak of O 1s was deconvoluted into two separate peaks in Fig. 4c. The lower binding energy peak at 530 eV, which is due to the metal oxide, corresponds to the Cu–O and V–O bonds while the higher binding energy peak at 531.6 eV is related to the oxygen of adsorbed hydroxyl on the surface [47]. Furthermore, Fig. 4d shows the high-resolution spectra of Cu 2p in CuO compound. The two peaks at approximately 934.6 and 954.3 eV are due to the Cu 2p_{3/2} and Cu 2p_{1/2}, respectively, confirming the presence of Cu²⁺ on the nanocomposite. In addition, the satellite peaks of Cu 2p_{3/2} and Cu 2p_{1/2} at about 943.2 and 962.8 eV are associated with the partially filled d-block (3d⁹) of Cu²⁺ and, thus, provide more evidence for the presence of CuO in nanocomposite [48]. In spectrum of V⁴⁺ (Fig. 4e), the peaks at 520.4 and 523.4 eV are due to V–O and V–OH, respectively. The presence of the VO₂ phase is confirmed by the combination of the V and O oxidation states due to the observation of V⁴⁺ [49].

Furthermore, using SDP V8 software, the atomic percentages of oxygen, titanium, copper, and vanadium elements were found to be 48.6%, 46.2%, 2.5%, and 2.7%, respectively.

3.5 HR-TEM

The structure of pristine and modified nanocomposite was studied using HR-TEM. Figure 5 shows the HR-TEM images of CuO-VO₂/TiO₂ nanocomposite. According to Fig. 5a–d and Figs S3(a and b), CuO-VO₂/TiO₂ nanocomposite displays nanotube shape and the nanosheets are deposited randomly on the surface of the nanotubes. The average inner diameter, external diameter of nanotubes, and length of nanosheets were found to be 5.80, 8.4, and 34 nm, respectively. The calculated d-space values were 0.32, 0.23, 0.32, and 0.35 nm corresponded to (110), (111), (110), and (101) planes of VO₂, CuO, rutile, and anatase phases of TiO₂, respectively. The results match the XRD pattern, XPS, and element distribution map analysis. It is well documented that long narrow channels play an important role in electron transferring, light conversion, and enhanced ion diffusion at the semiconductor interface from tubular depth and tube wall [50–54].

3.6 N₂ adsorption–desorption analysis

The N₂ adsorption–desorption isotherms of CuO-VO₂/TiO₂ nanocomposite are seen in Fig. 6a. The product obtained showed type IV isotherms with hysteresis loops, based on BDDT classification. It is noteworthy that the pore structures were analyzed

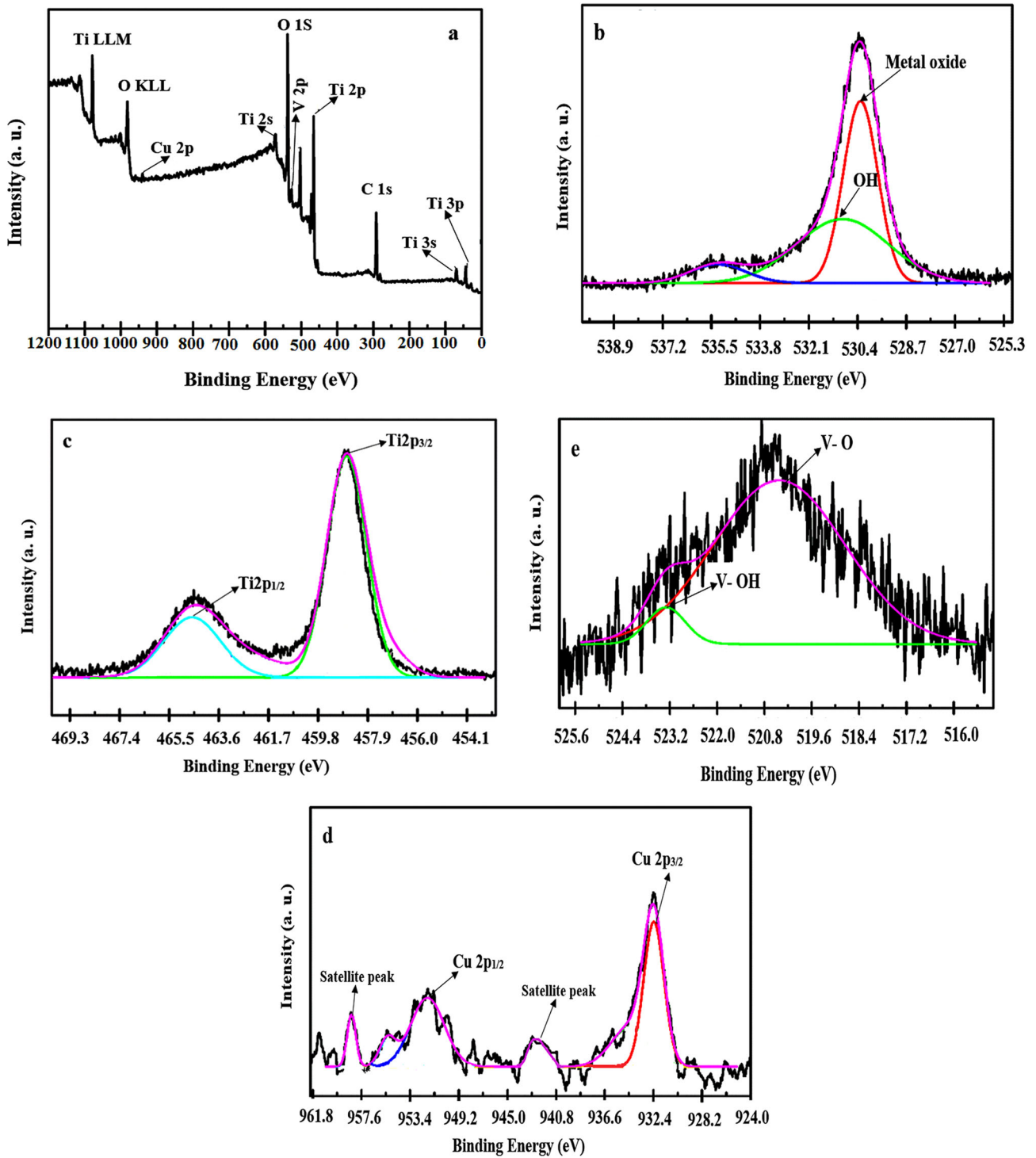


Fig. 4 XPS spectra of CuO-VO₂/TiO₂ nanocomposite (a) survey spectrum and high resolution of (b) O1s; (c) Ti2p; (d) Cu2p; and (e) V2p

further by the BJH method from N₂ adsorption–desorption isotherm (Fig. 6b). It should be pointed out that CuO-VO₂/TiO₂ nanocomposite shows a pore

size distribution at about 5.29 nm. The obtained inner diameter of nanotubes based on the HR-TEM was 5.80 nm; thus, the peak at 5.29 nm shows the pore

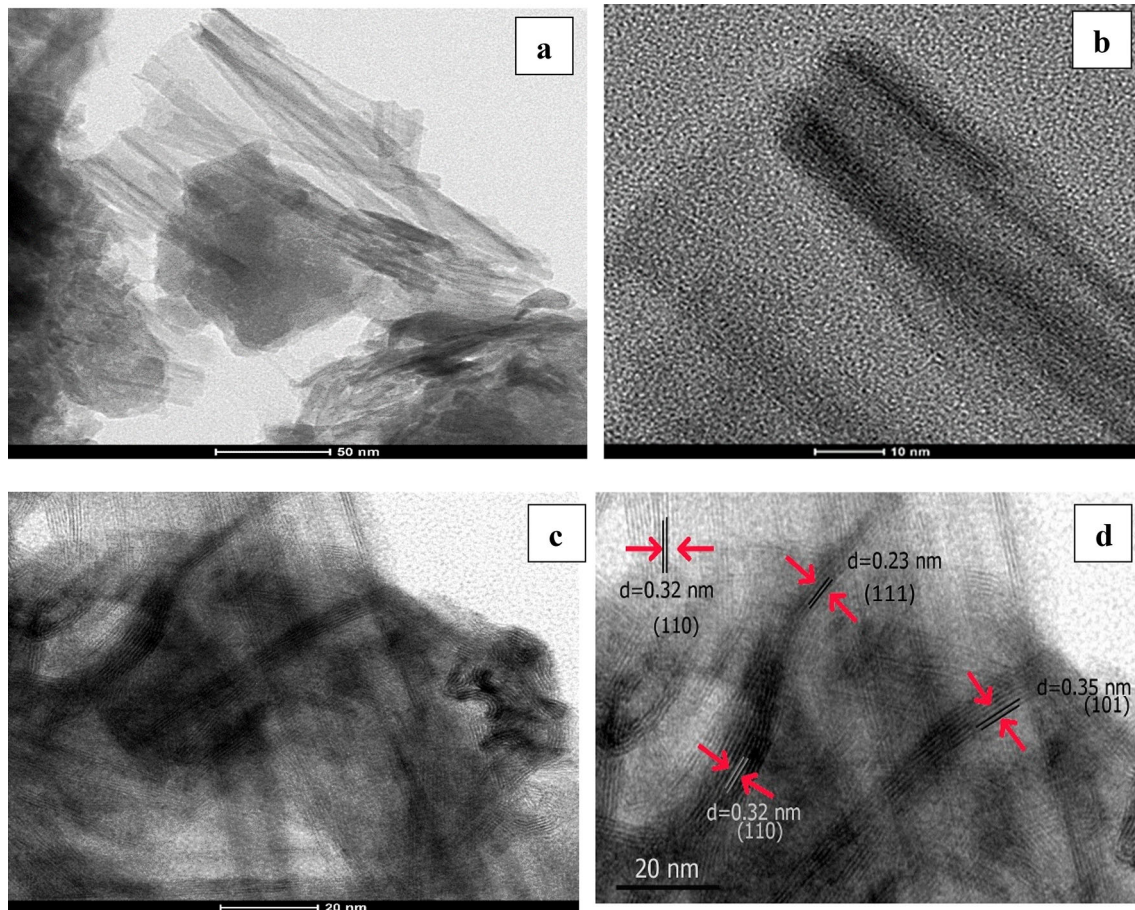


Fig. 5 HR-TEM of CuO-VO₂/TiO₂ nanocomposite

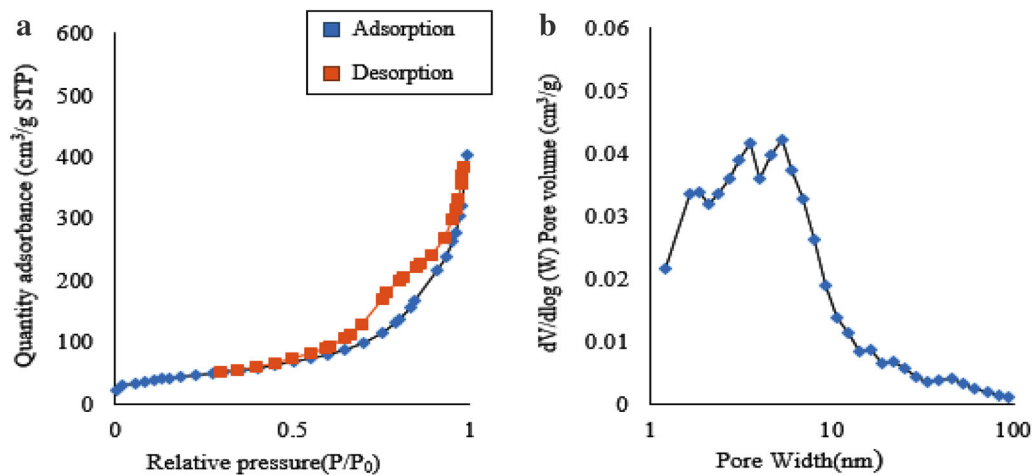


Fig. 6 **a** Isotherm of N₂ adsorption–desorption isotherms and **b** Particle size distribution of CuO-VO₂/TiO₂ nanocomposite

inner diameter of nanotubes. The BET surface area of CuO-VO₂/TiO₂ nanocomposite is quiet large (156.74 m²/g). The S_{BET} of CuO-VO₂/TiO₂ nanocomposite was clearly larger than bare TiO₂ (P-25). The results

of the BET and BJH analyses of CuO-VO₂/TiO₂ nanocomposite and TiO₂ (P-25) are summarized in Table 1 [55, 56].

Table 1 The results of the BET and BJH analysis of CuO-VO₂/TiO₂ nanocomposite and TiO₂(P-25)

Sample name	Pore size (nm)	Pore volume (cm ³ g ⁻¹)	S _{BET} (m ² g ⁻¹)
CuO-VO ₂ /TiO ₂ nanocomposite	5.29	0.606	156.74
TiO ₂ -P-25	21.0	50.0	50.0

3.7 UV–vis diffuse reflectance spectroscopy

Solid-state electronic spectra were applied to investigate the typical optical properties of CuO-VO₂/TiO₂ nanocomposite (Fig. 7a). In general, the band gap of semiconducting materials is determined by the Tauc plot as described in our last work [35].

The E_g of Cu-VO₂/TiO₂ nanocomposite was found as 2.5 eV with λ = 496 nm from Fig. 7b. This is smaller compared with TiO₂ (P-25) (3.2 eV). The p-n heterojunction semiconductor is obtained by connecting the n- and p-type semiconductors. In this case, the VB and CB energy edges of the n- and p-type semiconductors increase and decrease, respectively. The two semiconductors have close Fermi energy levels. In this work, TiO₂ and CuO/VO₂ are n- and p-type semiconductors, respectively. The electron/hole is generated in the CuO/VO₂ semiconductor during the irradiation by visible light because of its narrower band gap in comparison with TiO₂. Afterwards, the electron transfer to the CB edge of TiO₂ occurs due to the more positive potential of TiO₂ CB edge in comparison with CuO/VO₂ [57–59].

3.8 Mott–Schottky analysis

The charge transfer process of the composite junction was estimated using Mott–Schottky plots (Fig. 8). Typically, 2 mg of nanocomposite and 13 mg of 5 wt

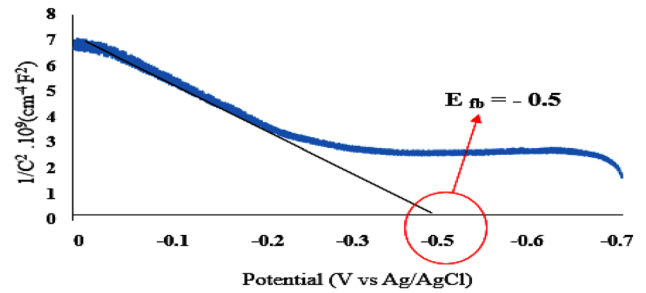
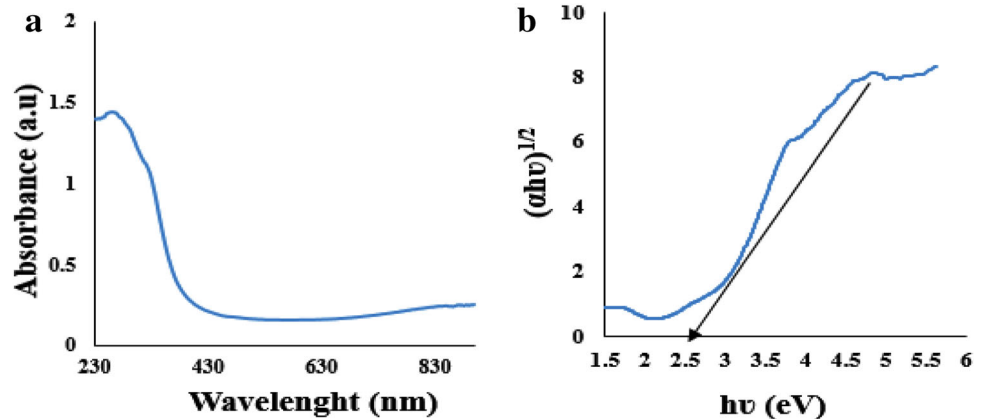


Fig. 8 The Mott–Schottky plot of CuO-VO₂/TiO₂ nanocomposite

percent of Nafion solution were dispersed in water/ethanol solvent mixture (3:1 v/v), subjected to ultrasonication for 15 min and then stirred for 24 h to obtain a homogeneous colloidal suspension. The CuO-VO₂/TiO₂ nanocomposite was deposited with 40 nm thickness on glass/ITO substrates at slow rates below 1 nm/s through thermal evaporation in vacuum Ag/AgCl couple, platinum electrode, and the prepared slides functioned as the reference, auxiliary, and working electrodes, respectively. A solution prepared of 0.1 M Na₂SO₄ was applied as electrolyte (pH 6.5). Plots of Mott–Schottky (impedance) were obtained in the dark with a 5 mV AC amplitude at the frequency and potential range of 100 Hz and -0.07–0 vs. Ag/AgCl, respectively. Equation (2) is used to drive the flat band potential (V_{fb}) and density of donor (N_d):

Fig. 7 (a) The absorption (b) plot of [αhv]^{1/2} vs. photon energy (hv) of CuO-VO₂/TiO₂ nanocomposite



$$\frac{1}{C^2} = \frac{2}{\varepsilon_0 \varepsilon_r e N_d} \left(V - V_{fb} - \frac{k_B T}{e} \right), \quad (2)$$

where N_d , ε_0 , ε_r , V , and T are the carrier density, permittivity in vacuum, relative permittivity, and applied potential is the absolute temperature, respectively. In addition, e and k_B are the electronic charge and Boltzmann constant, respectively. Therefore, a plot of $1/C^2$ vs. potential (V) will give a line of the extrapolation of which the x-axis will be attributed to the flat band potential of the semiconductor [60]. TiO_2 (P-25) shows a negative E_{fb} value (-0.62) [61] whereas in the case of $\text{CuO-VO}_2/\text{TiO}_2$, the E_{fb} values had a shift towards positive potential (-0.5 V). The generation of p - n junction between p -type co-catalyst (CuO , VO_2) and n -type TiO_2 is responsible for this positive shift of the E_{fb} potential. In addition, the position of the conduction band of $\text{CuO-VO}_2/\text{TiO}_2$ was $+0.1$ V (vs. RHE), and its valance band was located at 2.6 V (vs. RHE) (valance band calculated from $E_{VB} = E_{CB} + E_g$). The positions of the conduction band and valance bands of TiO_2 (P-25) were calculated as -0.1 and 3.1 V (vs. RHE), respectively [62]. Also, the donor density (N_d) of the $\text{CuO-VO}_2/\text{TiO}_2$ was estimated $8.197 \times 10^{20} \text{ cm}^{-3}$ using Eq. (2), while donor density for TiO_2 (P-25) was $3.47 \times 10^{20} \text{ cm}^{-3}$. The observed higher electron donor density of $\text{CuO-VO}_2/\text{TiO}_2$ could be due to a greater concentration of defects (TiO_2 properties such as light absorption, charge transport, and surface adsorption are closely associated with defect, which in turn plays an important part in TiO_2 photocatalytic performance. Of all the defects found in TiO_2 , oxygen vacancy, which has been extensively studied by both theoretical calculations and experimental characterizations, is one of the most significant and supposedly common defects in many metal oxides [63].) in the compound and/or better dispersion of $\text{CuO-VO}_2/\text{TiO}_2$ over TiO_2 (P-25) structure. The life of charge carriers can be extended by this improvement, which causes the recombination of ($e^- - h^+$) to decrease. Consequently, in the contact region, between TiO_2 and VO_2/CuO , the charge carrier density increases while the recombination of ($e^- - h^+$) decreases. These parameters are believed to be the main factor in the enhancement of photocatalytic reduction of dyes [64] (Fig. 9).

4 Photocatalytic activity

4.1 Photodegradation of MB, MO and CR

A 5 ml solution containing the dye (MB, MO, and CR (10 ppm)), 3 mg of $\text{CuO-VO}_2/\text{TiO}_2$ nanocomposite, and 1 mL of H_2O_2 (0.1 M) was stirred at ambient temperature, and the photocatalytic degradation of the dye was investigated under visible light. The maximum absorbances for MB, CR, and MO were 650, 500, and 450 nm, respectively. Linear plots are obtained by plotting $-\ln(A/A_0)$ of dye versus the irradiation time of the dye (in which A_0 and A are the absorbance values at $t = 0$ and time (t), respectively). Therefore, the photocatalytic dye degradation follows pseudo first-order kinetics. Thus, the slope of the plot of $-\ln(A/A_0)$ of the dye vs. irradiation time can be reasonably considered as the observed rate constants (k_{obs}) of the process of photocatalytic degradation. Decomposition of dyes was repeated for 4 cycles in the presence of nanocomposite. The results of recyclability of dyes are summarized in Table 2. At the same time (and within 1 h), the absorbance values of the dyes carried out in the dark were constant during 1 h. In addition to the absorbance due to the chemical decomposition of dyes, this experiment shows that there is not any absorbance via photodegradation in the solution.

In general, the active species during reaction are photogenerated holes (h^+), hydroxyl radicals ($\bullet\text{OH}$), and superoxide radicals ($\cdot\text{O}_2^-$). The effects of $\cdot\text{OH}$, $\cdot\text{O}_2^-$, and h^+ were investigated using EDTA, BQ, and IPA scavengers, respectively. The least dye degradation occurs in the presence of EDTA. Therefore, the main active species in the dye degradation process is the hydroxyl radical ($\bullet\text{OH}$). All photocatalytic degradation values, plots of $-\ln(A/A_0)$ of the dye vs. irradiation time, recyclability of $\text{CuO-VO}_2/\text{TiO}_2$ nanocomposite, and photodegradation efficiency (%) of the dye using different scavengers are shown in Figs. 9(a-d), Fig S4(a-d), and Fig S5(a-d) for MB, MO, and CR, respectively [65, 66].

Some previously reported about of photocatalytic degradation of dyes are shown in Table 3. According to this result, the best photocatalyst degradation of CR and MO under UV-Vis irradiation occurred at 30 and 35 min, respectively, for 2.5 ppm of dye using 5 mg of the catalyst. In contrast to the reported results, the time of degradation and amount of

Fig. 9 a Photocatalytic degradation under visible irradiation (b) plots of $-\ln(A/A_0)$ vs. irradiation time, (c) recyclability of CuO-VO₂/TiO₂ nanocomposite, and (d) photodegradation efficiency (%) of dye using different scavengers of MB

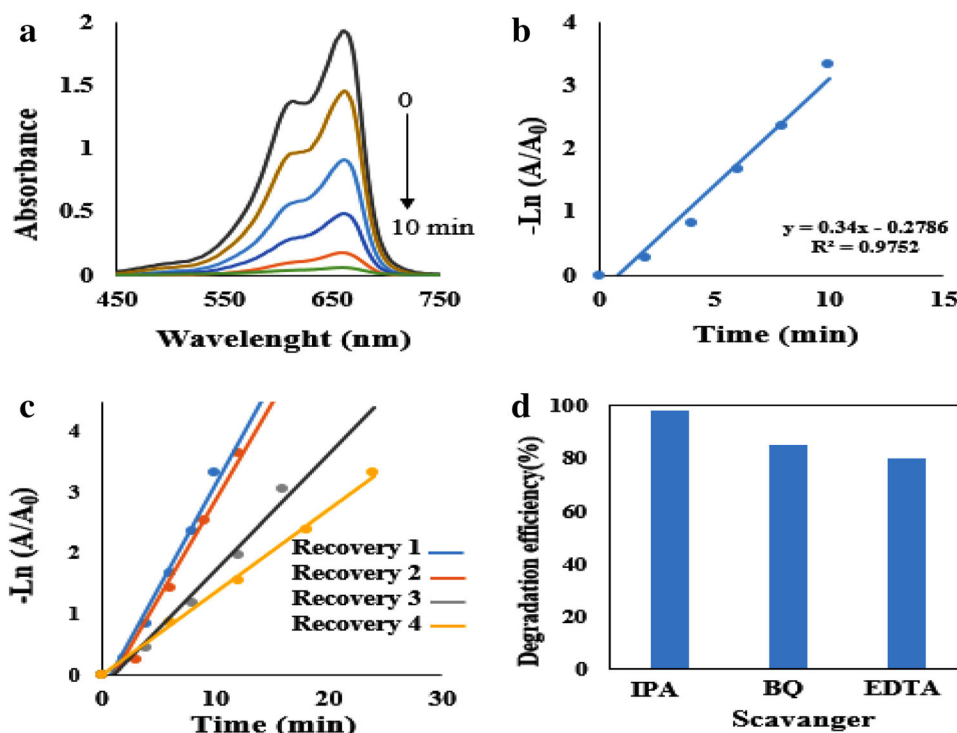


Table 2 Recovery of CuO-VO₂/TiO₂ nanocomposite in the degradation reaction of MB, Mo, and CR

Dye	MO	Time (min)	Kobs (min ⁻¹)
Dye	1	10	0.340
	2	12	0.320
	3	16	0.196
	4	24	0.136
MO	1	25	0.090
	2	30	0.066
	3	40	0.053
	4	50	0.035
MO	1	15	0.155
	2	20	0.106
	3	25	0.083
	4	36	0.056

catalyst in this work are suitable for decomposition of dyes [65–72].

4.2 Chemical oxygen demand analysis

An efficient method extensively used for the measurement of the organic amount of wastewater is the chemical oxygen demand test. The amount of the waste is measured by the test with respect to the total required oxygen for the oxidation of organic matter

to water and CO₂. In this work, COD results were used as a parameters to evaluate the photocatalyst. In this experiment, the dye (MB, CR, and MO) solutions (50 ml) and CuO-VO₂/TiO₂ nanocomposite (0/01gr) were subjected to the visible light for 2 h. After photodegradation of the dyes, the samples were centrifuged for 10–15 min, and the absorbance was recorded. The percentage removal of COD of the three dyes was estimated using Eq. 1. It was observed that the COD values of the different dyes decreased from 880 to 6.8 mg L⁻¹, 640 to 13.8 mg L⁻¹, and 750 to 18.8 mg L⁻¹ for MB, CR, and MO, respectively. The values of the percentage removal of COD were 99%, 98%, and 97.5% for MB, CR, and MO, respectively. The final results show that the mineralization of dyes was performed successfully [73, 74].

4.3 Zeta potential analysis

The major characteristic factor for the determination of the colloidal stability of a catalyst suspension, which also affects the catalytic efficiency, is the surface charge (zeta potential). Adsorption of dye molecules is related to surface charge of catalyst, and the interaction between the molecules of dye and catalyst surface is changed during the change of surface charge. A 10 mg/L solution of the catalyst

Table 3 Degradation of dyes with other catalysts

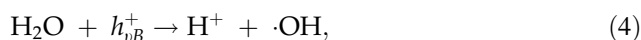
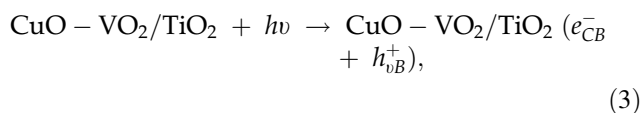
Catalyst	Dye	Concentration (ppm)	Amount of catalyst	Time of photodegradation(min)	Source of light	Reference
PbTiO ₂	CR	10	5 mg	150	Visible	[66]
ZnO-TiO ₂ nanocomposite	MB	5	0.2 gr	180	UV	[67]
TiO ₂ /BiVO ₄	MB	10	0.1 gr	180	Visible	[68]
TiO ₂ nanoparticle	MO	2.5	5 mg	30	UV/Visible	[69]
	CR	2.5	5 mg	120	UV/Visible	
Pd-doped TiO ₂	MO	20	1.5 gr	180	UV	[70]
	MB	20	1.5 gr	120	UV	
TiO ₂ /Al ₂ O ₃	MO	20	5 mg	100	UV	[71]
Silica-TiO ₂	MO	20	1 gr	80	UV	[72]
CuO-VO ₂ /TiO ₂ nanocomposite	MB	10	3 mg	10	Visible	This
	MO	10	3 mg	15	Visible	research
	CR	10	3 mg	15	Visible	

was prepared using deionized water to determine the zeta potential of the nanocomposite. According to zeta-potential measurement (-91.0 mV) (Fig. S6), CuO-VO₂/TiO₂ nanocomposite carries a negative charge, and there is an electrostatic attraction between the cationic dye molecules and negatively charged photocatalyst surface. The degradation time and rate constant results were better for both CR and MB cationic dyes compared to MO anionic dye. This can be attributed to the better electrostatic attraction between the cationic dye and the negatively charged catalyst [75, 76].

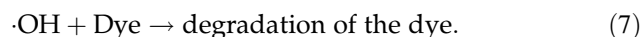
4.4 Mechanism of photocatalyst

The XPS analysis showed the presence of CuO and VO₂ in the nanocomposite. Cu²⁺ and V⁴⁺ are the major species, which are responsible for the variation of the optical properties of the nanocomposite. Electron-hole pairs are formed on the TiO₂ and CuO-VO₂/TiO₂ surfaces upon the illumination of visible light. The photoexcited charge carriers are capable of recombination and participation in the photocatalytic reaction [77, 78]. The conduction and valence band edge values of TiO₂, an n-type semiconductor, are 3.2 and -0.1 eV, respectively [79]. However, the corresponding values for CuO-VO₂, a p-type semiconductor, are $+0.1$ and 2.96 eV, respectively, according to the Mott-Schottky analysis [79]. The presence of CuO and VO₂ in the nanocomposite decreases the band gap to 2.5 eV, which is appropriate for the absorbance of visible light in photocatalytic reactions

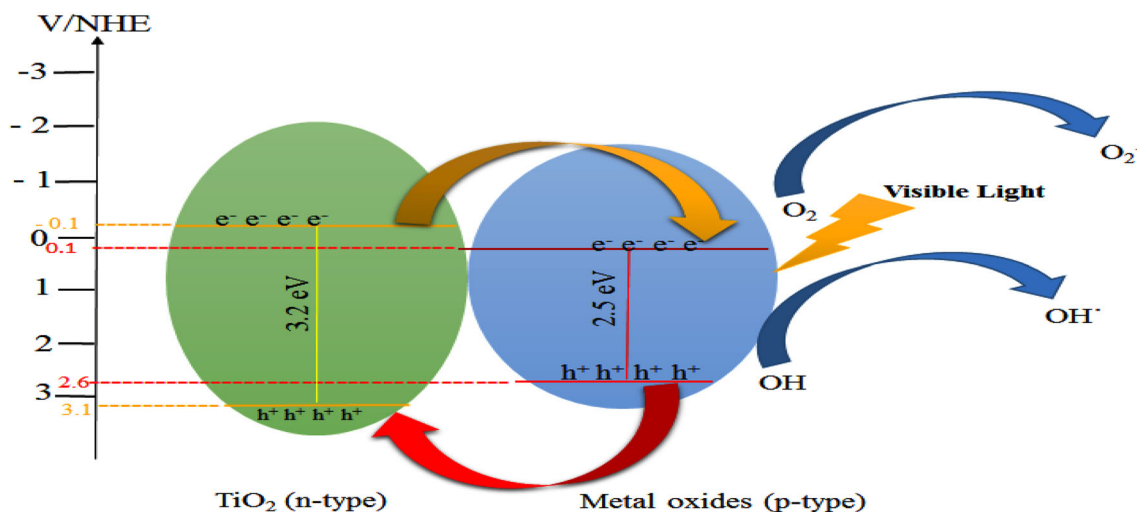
(Fig. 12a). The electron from TiO₂ conduction band moves to the conduction band of metal oxides while the hole migrates in the opposite direction. In addition, the p-n junction is formed by TiO₂ and the metal oxides. The charge carriers formed on various heterojunction sites react with the oxygen and water adsorbed on the surface of the catalyst to form superoxide and hydroxyl radicals. (Scheme 2) [80, 81]. Based on the results of scavenging, hydroxyl radical ($\cdot\text{OH}$) was an active reagents in the oxidation of organic materials. Water and oxygen change to radicals by reaction with hole, respectively, (Eqs. 3–7) [82].



But these radicals are not sufficient and through reaction of light with H₂O₂ molecules, hydroxyl radicals produced in the reaction media (Eq. 4).



The production of hydroxyl radicals, which are apparently the main reason for the mineralization of organic compounds, is accounted for by the holes in the valence band (Eq. 5).



Scheme 2 Schematic diagram for p-n heterojunction formation in the CuO-VO₂/TiO₂ nanocomposite and the excitation and transfer process for charge carriers in the CuO-VO₂/TiO₂ nanocomposite under visible-light irradiation

5 Conclusions

In summary, CuO-VO₂/TiO₂ nanocomposite was prepared via hydrothermal method. The structure of the synthesized compound was investigated by different spectroscopic methods. EDX was used to confirm the presence of V, Cu, and Ti. The V⁴⁺ was present as VO₂ in the nanocomposite. The pure TiO₂ anatase phase was converted to more photoactive anatase and rutile mixed phases. The morphology of the nanosheets/nanotubes was established for the novel compound. CuO-VO₂ was incorporated into the TiO₂ to prepare a p-n semiconductor with low band gap and high photocatalytic activity. In addition, by reducing the band gap in this p-n semiconductor, the photocatalytic degradation of MB, CR, and MO was carried out in the visible-light region. Unlike the reported photocatalysts, the novel composite is more active toward degradation of contaminants. Dye degradation occurred in the presence of hydroxyl radical as the major active species. Based on COD the analysis, the degraded dyes were significantly mineralized.

Acknowledgements

This work was financially supported by Isfahan University of Technology. We are thankful to our colleagues from Isfahan University of Technology for their insight and expertise.

Declarations

Conflict of interest The authors declare no known competing financial interests or personal relationships, which could affect the work reported in this paper.

Supplementary Information: The online version contains supplementary material available at <http://doi.org/10.1007/s10854-021-06486-1>.

References

1. T. Chankhanittha, J. Watcharakitti, S. Nanan, *J. Mat. Sci. Materials EL* **30**, 17804–17819 (2019)
2. I. Khan, M. Usman, M. Imran, K. Saeed, *J. Mat. Sci. Materials EL* **23** (2020).
3. VP. Kasperchik, AL. Yaskevich, AV. Bil'Dyukevich, *Pet. Chem* **52**, 545–56 (2012).
4. L. Chang, Y. Cao, G. Fan, C. Li, W. Peng, *RSC Adv* **9**, 20226–20239 (2019)
5. M.R. Gaddekar, M.M. Ahammed, *Desalin Water Treat* **52**, 6392–6400 (2016)
6. N.H. Hoong, N. Ismail, *EDP. Sci* **152**, 01008 (2018)
7. Y. Deng, R. Zhao, *Curr. Pollut. Rep* **1**, 167–176 (2015)
8. J. Parhizkar, M.H. Habibi, *J. Water Environ. Nanotechnol* **4**, 17–30 (2019)
9. L. Sun, 2015. Study of Photochemical Formation of Hydroxyl Radical in Natural Waters.
10. EM. Cuerda-Correa, *Water* **12**, 102 (2020).
11. D. Dastan, *Appl. Phys. A* **123**, 699 (2017)

12. Z. Rahmani, M. Kermani, M. Gholami, A.J. Jafari, N.M. Mahmoodi, *J. Environ. Health Sci. Eng* **9**, 14 (2012)
13. S. Abbasi, M. Hasanpour, F. Ahmadpoor, M. Sillanpää, D. Dastan, A. Achour, *Int. J. Environ. Anal. Chem* **13**, 1–7 (2019)
14. M.M. Khan, S.A. Ansari, D. Pradhan, M.O. Ansari, J. Lee, N.H. Cho, *J. Mat. Chem. A* **2**, 637–644 (2014)
15. O.R. Fonseca-Cervantes, A. Pérez-Larios, V.H. Romero Arellano, B. Sulbaran-Rangel, C.A. Guzmán González, *Processes* **8**, 1032 (2020)
16. A.A. Isari, A. Payan, M. Fattahi, S. Jorfi, B. Kakavandi, *Appl. Sur. Sci* **462**, 549–564 (2018)
17. M. Anas, D.S. Han, K. Mahmoud, H. Park, A. Abdel-Wahab, *Mat. Sci. Semicon* **41**, 209–218 (2016)
18. N. Riaz, F.K. Chong, Z.B. Man, M.S. Khan, B.K. Dutta, *Ind. Eng. Chem. Res* **52**, 4491–4503 (2013)
19. N. Riaz, C.F. Kait, Z. Man, B.K. Dutta, R.M. Ramli, M.S. Khan, *J. Adv. Mater. Res* **917**, 151–159 (2014)
20. D.P. Kumar, N.L. Reddy, M. Karthik, B. Neppolian, J. Madhavan, M.V. Shankar, *Sol. Energy Mater Sol. Cells* **154**, 78–87 (2016)
21. M.R. Bayati, F. Golestani-Fard, A.Z. Moshfegh, *Catal. Lett* **134**, 162–168 (2010)
22. M.H. Habibi, E. Shojaee, *Spectrochim Acta A Mol Biomol Spectrosc* **229**, 117796 (2020)
23. P. Kar, Y. Zhang, N. Mahdi, U.K. Thakur, B.D. Wiltshire, R. Kisslinger, K. Shankar, *Nanotechnology* **29**, 01400 (2017)
24. S. Mathew, P. Ganguly, S. Rhatigan, V. Kumaravel, C. Byrne, S.J. Hinder, J. Bartlett, M. Nolan, S.C. Pillai, *Appl. Sci* **8**, 2067 (2018)
25. M. Jasim, O.A.A. Dakhil, E.H. Hussein, H.I. Abdullah, *J Mater. Sci.: Mater. Electron* **31**, 10707–10714 (2020)
26. N.R. Dhineshbabu, V. Rajendran, N. Nithyavathy, R. Vetumperumal, *Appl. Nano. Sci* **6**, 933–939 (2016)
27. T. Tangcharoen, W. Klysubun, C. Kongmark, *J. Mat. Sci. Materials EL* **31**, 12807–12822 (2020)
28. C. Lamsal, N.M. Ravindra, *J. Mat. Sci* **48**, 6341–6351 (2013)
29. J. Kong, Y. Wang, Q. Sun, D. Meng, *J. Elec. Mat* **46**, 4791–4797 (2017)
30. Y. Wang, Y. He, Q. Lai, M. Fan, *J. Environ. Sci. Int* **26**, 2139–2177 (2014)
31. W. Wang, J. Zhang, D. Liang, Y. Li, Y. Xie, Y. Wang, J. Li, *J. Mat. Sci. Materials EL* **31**, 8844–8851 (2020)
32. A.H. Kianfar, M.V. Arayesh, *J. Environ. Chem. Eng* **8**, 103640 (2020)
33. A.H. Kianfar, P. Dehghani, M.M. Momeni, *J. Mater. Sci. Mater. EL* **27**, 3368–3375 (2016)
34. M. Dostani, A.H. Kianfar, M.M. Momeni, *J. Mater. Sci. Mater. EL* **28**, 633–40 (2017)
35. Z.M. Shammi, A.H. Kianfar, M.M. Momeni, *J. Mater. Sci. Mater. EL* **31**, 14810–14822 (2020)
36. M.A. Zavala, S.A. Morales, M. Ávila-Santos, *Heliyon* **3**, 00456 (2017)
37. D.A. Aljuboury, P. Palaniandy, H.B. Abdul Aziz, S. Feroz, S.S. Abu Amr, *Water Sci. Technol* **74**, 1312–25 (2016)
38. Y.H. Chiu, T.F. Chang, C.Y. Chen, M. Sone, Y.J. Hsu, *Catalysts* **9**, 430 (2019)
39. E.M. Rodríguez, G. Márquez, M. Tena, P.M. Álvarez, F.J. Beltrán, *Appl. Cat. B. Environ* **178**, 44–53 (2015)
40. M. Shahrezaei, S. Habibzadeh, A.A. Babaluo, H. Hosseinkhani, M. Haghghi, A. Hasanzadeh, R. Tahmasebpour, *J Exp Nanosci* **12**, 45–61 (2017)
41. K.C. Sun, M.B. Qadir, S.H. Jeong, *RSC. Adv* **4**, 23223–23230 (2014)
42. Y. Zhang, J. Chen, X. Li, *Catal. Lett* **139**, 129–133 (2010)
43. O. Frank, M. Zukalova, B. Laskova, J. Kürti, J. Koltai, L. Kavan, *Phys. Chem. Chem. Phys* **14**, 14567–14572 (2012)
44. Y. Zeng, T. Wang, S. Zhang, Y. Wang, Q. Zhong, *Appl. Surf. Sci* **411**, 227–234 (2017)
45. C.Y. Xu, P.X. Zhang, L. Yan, *J. Raman spectrosc* **32**, 862–865 (2001)
46. M. Yang, Y. Yang, B. Hong, L. Wang, K. Hu, Y. Dong, H. Xu, H. Huang, J. Zhao, H. Chen, L. Song, *Sci. reports* **6**, 23119 (2016)
47. A. Kubiak, Z. Bielan, M. Kubacka, E. Gabała, A. Zgoła-Grzeškowiak, M. Janczarek, M. Zalas, A. Zielińska-Jurek, K. Siwińska-Ciesielczyk, T. Jesionowski, *Appl. Sur. Sci* **18**, 146344 (2020)
48. G. Panzeri, M. Cristina, M.S. Jagadeesh, G. Bussetti, L. Magagnin, *Sci. Rep* **10**, 1 (2020)
49. J. Wang, X. Zhang, Y. Zhang, A. Abas, X. Zhao, Z. Yang, Q. Su, W. Lan, E. Xie, *RSC Adv* **7**, 35558–35564 (2017)
50. X. Zhang, L. Wang, C. Liu, Y. Ding, S. Zhang, Y. Zeng, Y. Liu, S. Luo, *J. Hazard. Mater* **313**, 244–252 (2016)
51. T.N. Trang, L.T. Tu, T.V. Man, M. Mathesh, N.D. Nam, V.T. Thu, *Compos. B. Eng* **174**, 106969 (2019)
52. L.Q. Lu, Y. Wang, *J. Mat. Chem* **21**, 17916–17921 (2011)
53. U. Bharagav, N.R. Reddy, V.N. Koteswararao, P. Ravi, M. Sathish, K.K. Cheralathan, M.V. Shankar, M.M. Kumari, *Energy Fuels* **34**, 14598–14610 (2020)
54. D.P. Kumar, N.L. Reddy, B. Srinivas, V. Durgakumari, V. Roddatis, O. Bondarchuk, M. Karthik, Y. Ikuma, M.V. Shankar, *Sol. Energy Mater Sol. Cells* **146**, 63–71 (2016)
55. X. Wei, G. Zhu, J. Fang, J. Chen, *Int. J. of Photoenergy* **1**, 2013 (2013)
56. G. Arthi, J. Archana, M. Navaneethan, S. Ponnusamy, Y. Hayakawa, *Int. J. Chemtech Res* **7**, 1563–1568 (2015)
57. N. Saha, A. Sarkar, A.B. Ghosh, A.K. Dutta, G.R. Bhadu, P. Paul, B. Adhikary, *RSC Adv* **5**, 88848–88856 (2015)

58. H. Nishikiori, N. Harata, S. Yamaguchi, T. Ishikawa, H. Kondo, A. Kikuchi, K. Teshima, *Catalysts* **9**, 383 (2019)
59. M. Janczarek, E. Kowalska, *Catalysts* **7**, 317 (2017)
60. M. Madkour, O.G. Allam, A.A. Nazeer, M.O. Amin, E. Al-Hetlani, *J. Mat. Sci. Materials EL* **30**, 10857–10866 (2019)
61. N.M. Mohamed, R. Bashiri, F.K. Chong, S. Sufian, S. Kakooei, *Int. J. Hydrog. Energy* **40**, 14031–14038 (2015)
62. D. Guerrero-Araque, D. Ramirez-Ortega, H.A. Calderon, J.M. Saniger, R. Gómez, *Top. Cat* **20**, 1–9 (2020)
63. X. Pan, M.Q. Yang, X. Fu, N. Zhang, Y.J. Xu, *Nanoscale* **5**, 3601–3614 (2013)
64. S.J. Moniz, J. Tang, *Chem. Cat. Chem* **7**, 1595 (2015)
65. P.W. Koh, L. Yuliaty, S.L. Lee, *J. Teknol* **69**, (2014).
66. U.O. Bhagwat, J.J. Wu, A.M. Asiri, S. Anandan, *Chemistry Select* **3**, 11851–11858 (2018)
67. W.T. Kim, K.H. Na, D.C. Park, W.H. Yang, W.Y. Choi, *J. Nanomater* **10**, 1311 (2020)
68. M.F. Samsudin, S. Sufian, R. Bashiri, N.M. Mohamed, L.T. Siang, R.M. Ramli, *Mater. Today* **5**, 21710–21717 (2018)
69. D. Ljubas, G. Smoljanić, H. Juretić, *J. Environ. Manage* **161**, 83–91 (2015)
70. C.H. Nguyen, C.C. Fu, R.S. Juang, *J. Clean. Prod* **202**, 413–427 (2018)
71. M. Pakmehr, A. Nourmohammadi, M. Ghashang, A. Saffar Teluri, *Int. J. Food Sci. Technol* **1**, 31–8 (2015).
72. Y. Guo, S. Yang, X. Zhou, C. Lin, Y. Wang, W. Zhang, *J. Nanomater* **1**, 2011 (2011)
73. S. Venkatesh, A.R. Quaff, N.D. Pandey, K. Venkatesh, *Desalin. Water. Treat* **57**, 4135–4145 (2016)
74. L.N. Du, G. Li, F.C. Xu, X. Pan, L.N. Wen, Y. Wang, *Water. Sci. Technol* **69**, 2004–2013 (2014)
75. R. Sankar, P. Manikandan, V. Malarvizhi, T. Fathima, K.S. Shivashangari, V. Ravikumar, *Spectrochim. Acta. A. Mol. Biomol. Spectrosc* **121**, 746–750 (2014)
76. P. Borthakur, M.R. Das, *J. colloid. Inte. sci* **516**, 342–354 (2018)
77. X. Zhang, L. Zhang, T. Xie, D. Wang, *J. Phys. Chem. C* **113**, 7371–7378 (2009)
78. G. Yang, D. Chen, H. Ding, J. Feng, J.Z. Zhang, Y. Zhu, S. Hamid, D.W. Bahnemann, *Appl. Catal. B* **219**, 611–618 (2017)
79. G. Yang, H. Ding, J. Feng, Q. Hao, S. Sun, W. Ao, D. Chen, *Sci. rep* **7**, 1–9 (2017)
80. Y. Lv, H. Liu, W. Zhang, S. Ran, F. Chi, B. Yang, A. Xia, *J. Environ. Chem. Eng* **1**, 526–533 (2013)
81. Z. Li, H. Chen, W. Liu, *Catalysts* **8**, 557 (2018)
82. M. Movahedi, A.R. Mahjoub, S. Janitabar-Darzi, *J. Iran. Chem. Soc* **6**, 570–577 (2009)

Publisher's Note Springer Nature remains neutral with regard to jurisdictional claims in published maps and institutional affiliations.